

Supplementary Information

Unambiguous Determination of Crystal Orientation in Black Phosphorus by Angle-resolved Polarized Raman Spectroscopy

Bo Zou,^{#a} Yadong Wei,^{#b} Yan Zhou,^c Dingning Ke,^d Xu Zhang,^a Meng Zhang,^a
Cho-Tung Yip,^a Xiaobin Chen,^a Weiqi Li,^{*b} and Huarui Sun^{*a}

^a School of Science and Ministry of Industry and Information Technology Key Laboratory of Micro-Nano Optoelectronic Information System, Harbin Institute of Technology, Shenzhen, 518055, China

^b School of Physics, Harbin Institute of Technology, Harbin 150001, China

^c Center for High Pressure Science & Technology Advanced Research, Shanghai 201203, China

^d Experiment and Innovation Center, Harbin Institute of Technology Shenzhen Graduate School, Shenzhen, 518055, China

[#] B. Zou and Y. Wei contributed equally to this work.

Calculations

Semi-classical model for angle-resolved Raman intensities. Since the Raman tensor is described as the derivative of a complex dielectric matrix with respect to normal coordinates of crystals (eqn (3)), the Raman tensors should also be complex for opaque absorbent materials including BP (i.e. considering linear dichroism effect). In addition, when the absorption coefficient is relatively large and the scattering depth is not deep enough, the birefringence effect can be neglected.¹

According to the group theory, bulk BP crystal belongs to point group D_{2h} . And three Raman active modes, A_g^1 , B_{2g} , and A_g^2 , are allowed in the backscattering geometry. The associated Raman tensors are given by²

$$R(A_g^j) = \begin{pmatrix} a_j e^{i\phi_a} & 0 & 0 \\ 0 & b_j e^{i\phi_b} & 0 \\ 0 & 0 & c_j e^{i\phi_c} \end{pmatrix} R(B_{2g}) = \begin{pmatrix} 0 & 0 & f e^{i\phi_f} \\ 0 & 0 & 0 \\ f e^{i\phi_f} & 0 & 0 \end{pmatrix}, \quad (S1)$$

where $j = 1, 2$ represents the A_g^1 and A_g^2 phonon modes, respectively. $a(\phi_a)$, $b(\phi_b)$, $c(\phi_c)$, $f(\phi_f)$ are the amplitudes (phases) of the Raman tensor elements, respectively, and can be obtained either from DFT calculations shown in Table SIII or by fitting the experimental data. The finite phases stem from the anisotropic absorption of BP. According to the Raman selection rule, the intensity of the Raman modes can be calculated using:

$$I(\theta, \gamma) \propto |\hat{e}_i \cdot R \cdot \hat{e}_s|^2, \quad (S2)$$

where \hat{e}_i and \hat{e}_s are the light polarization unitary vectors of the incident and scattered light, respectively, θ is the angle between the incident laser polarization and the ZZ direction, and γ is the angle between \hat{e}_i and \hat{e}_s .

In the parallel polarization configuration ($\gamma = 0^\circ$), the Raman intensity is given by:

$$I_{//}(A_g) = a^2 \sin^4 \theta + c^2 \cos^4 \theta + 2ac \sin^2 \theta \cos^2 \theta \cos \phi_{ca}, \quad (S3)$$

$$I_{//}(B_{2g}) = f^2 \sin^2 2\theta. \quad (S4)$$

In the vertical polarization configuration ($\gamma = 90^\circ$), the Raman intensity is given by:

$$I_{\perp}(A_g) = (a^2 + c^2 - 2ac \cos \phi_{ca}) \sin^2 \theta \cos^2 \theta, \quad (S5)$$

$$I_{\perp}(B_{2g}) = f^2 \cos^2 2\theta, \quad (S6)$$

where $\phi_{ca} = \phi_c - \phi_a$ is the phase difference between the Raman tensor elements c and a . In this work, we only focus on the two A_g modes.

When the incident laser polarization is along the ZZ direction ($\theta = 0^\circ$) and AC direction ($\theta = 90^\circ$), $I_{//}(A_g) = c^2$ and a^2 , respectively. This expression relates the Raman intensity to the Raman tensor element, and it is convenient to display experimental data while avoiding experimental uncertainty to a certain extent.

Supporting Figures

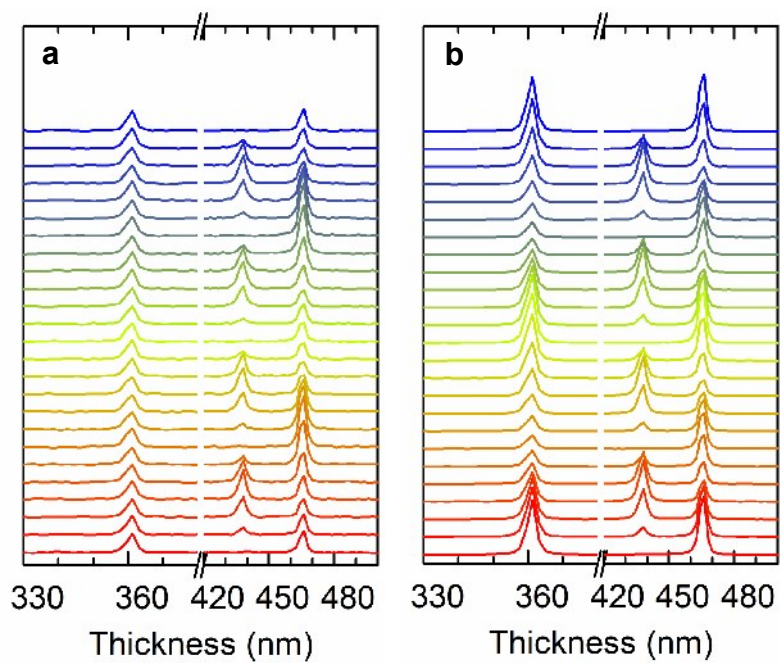


Fig. S1. Angle-dependent Raman spectra corresponding to data in Fig. 1g, h for **(a)** ~ 40 nm and **(b)** ~ 70 nm BP areas using a 532 nm laser. The spectra are shown in 15-degree increments.

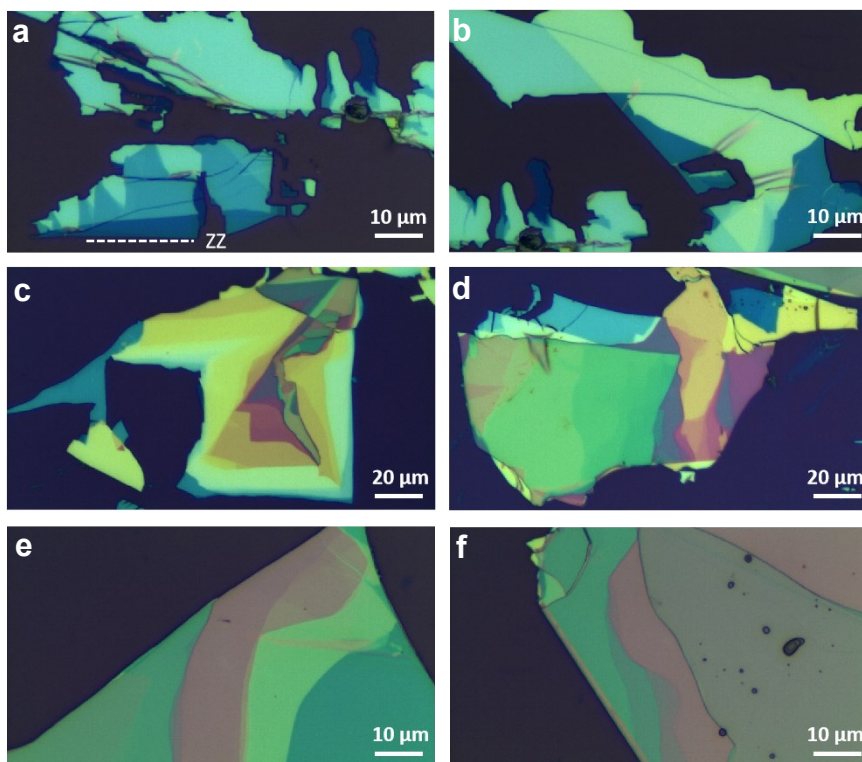


Fig. S2. Optical images of BP flakes exfoliated on SiO₂ (300 nm)/Si substrates for ARPRS measurements.

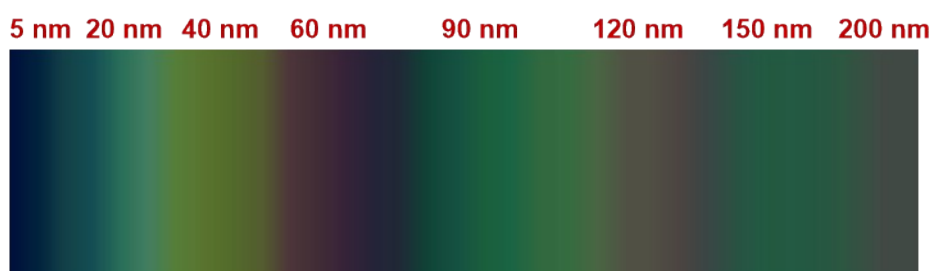


Fig. S3. A color bar of BP flakers whose RGB parameters are extracted from Fig. S2 and the thicknesses are determined by the atomic force microscope. The thickness increases from left (5 nm) to right (200 nm).

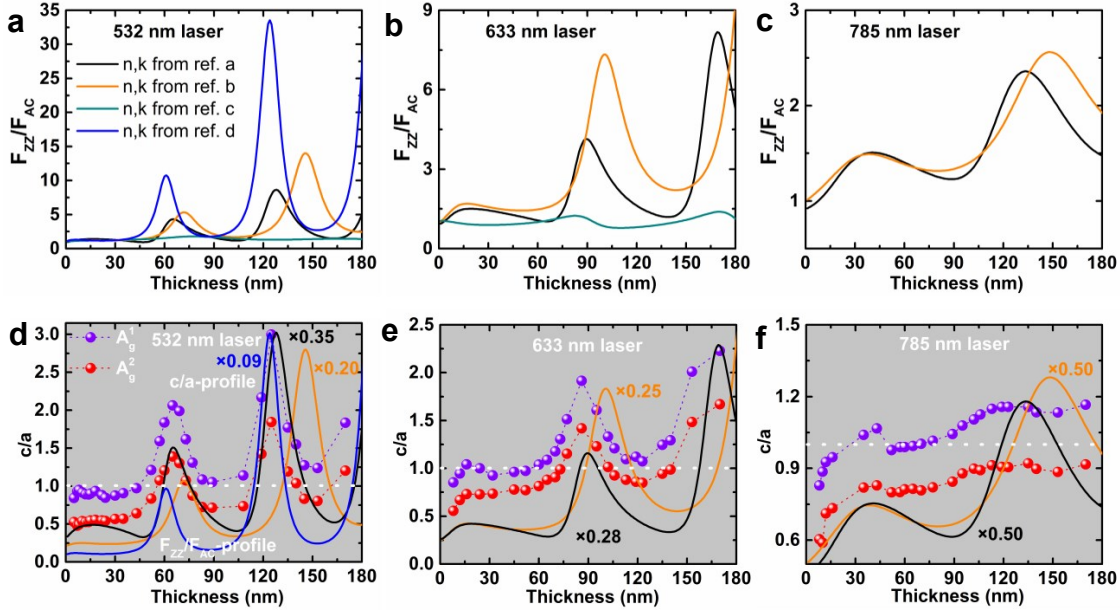


Fig. S4. Calculated interference enhancement factor ratio (F_{ZZ}/F_{AC}) as a function of the BP thickness on a SiO_2 (300 nm)/Si substrate for (a) 532 nm, (b) 633 nm, and (c) 785 nm lasers by using the refractive index values of BP from four references. Fitting of the reduced F_{ZZ}/F_{AC} -profiles with the experimental results for (d) 532 nm, (e) 633 nm, and (f) 785 nm lasers.

There are some experimental or theoretical reports on the complex refractive index of BP; however, they are to some extent inconsistent with each other. Therefore, we tried the different refractive index data of BP reported in four literatures to fit our experimental results. They are the experimental values based on electron energy-loss spectroscopy measurement (ref. a)³, incident angle-resolved laser reflectivity measurement (ref. d)⁴, optical contrast spectra measurement (ref. c)⁵ and the theoretical values (ref. b)⁶. The interference enhancement factor profiles (F_{ZZ}/F_{AC} -profiles) of BP flakes calculated based on the refractive index values in these documents and their fittings with our experimental results are shown in Fig. S4. We can clearly see that the F_{ZZ}/F_{AC} -profiles calculated with the refractive index data from ref. a are in best agreement with our experimental results for all laser wavelengths, especially the interference peak position. The peak positions of the F_{ZZ}/F_{AC} -profiles calculated using the refractive index data from ref. b are greater than our experimental results, and the peak positions of the F_{ZZ}/F_{AC} -profiles calculated using the refractive index data from ref. c are smaller (in nm). The F_{ZZ}/F_{AC} -profiles calculated using the refractive index data from ref. d is in worst agreement with the experimental results. In addition, ref. c only provides refractive index

data at 532 nm, ref. d provides refractive index data in the range of 475-650 nm, and refs. a and b provide wavelength-dependent refractive index data in the range of 0-10 eV and 0-24.5 eV, respectively, which fully span the laser wavelengths used in our experiment. Therefore, we adopt the refractive index data of ref. a to calculate the F_{ZZ}/F_{AC} - profiles, which is different from the widely used data of ref. b.

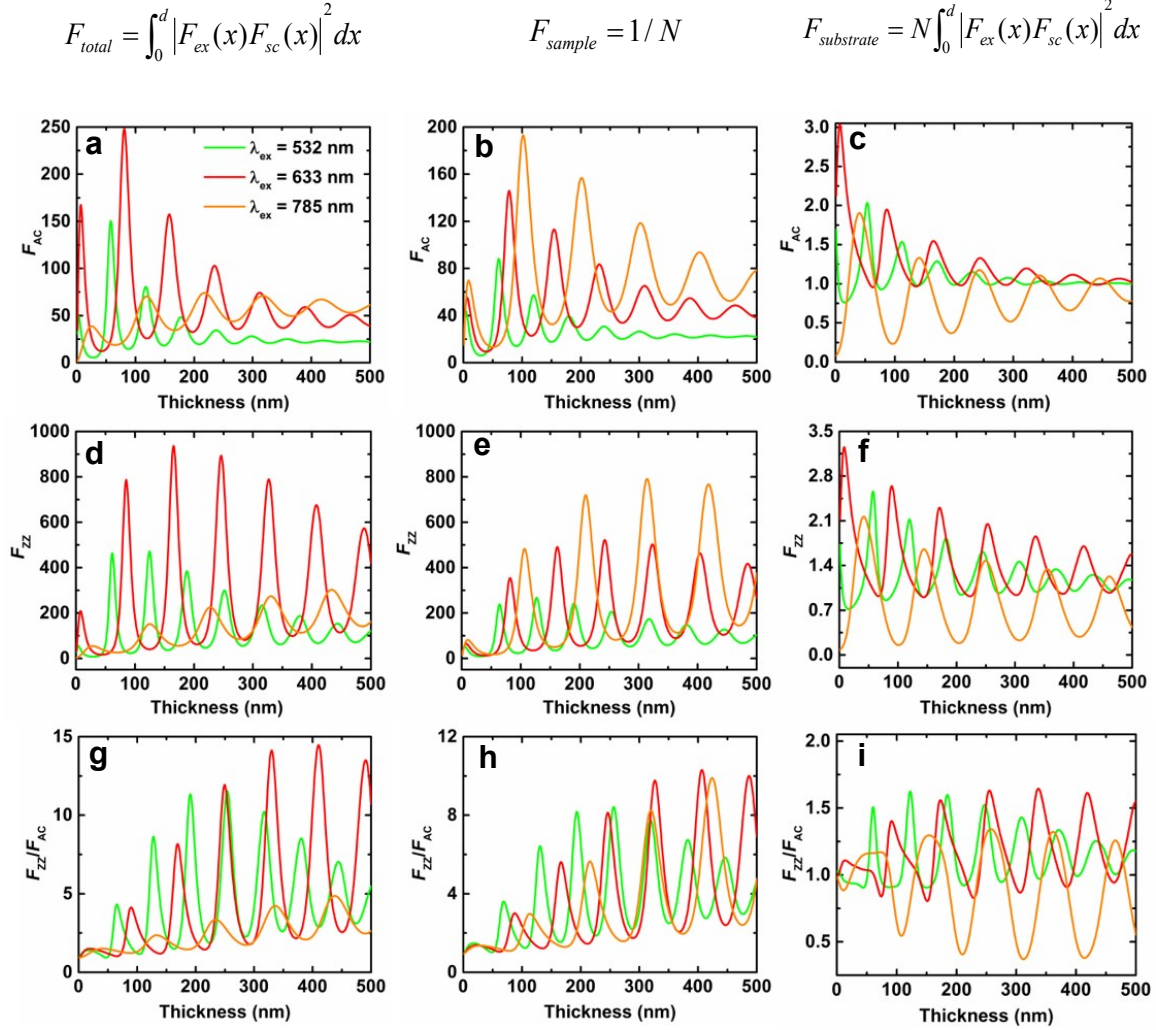


Fig. S5. Calculated excitation-wavelength dependent F_{AC} , F_{ZZ} , and F_{ZZ}/F_{AC} (**a,d,g**) by

$$F_{total} = \int_0^{d_1} |F_{ex}(x)F_{sc}(x)|^2 dx, \quad (\mathbf{b,e,h}) \quad \text{by} \quad F_{sample} = 1/N \quad \text{and} \quad (\mathbf{c,f,i}) \quad \text{by}$$

$$F_{substrate} = N \int_0^{d_1} |F_{ex}(x)F_{sc}(x)|^2 dx, \quad \text{respectively, as a function of the sample thickness for}$$

BP on a SiO₂ (300 nm)/Si substrate.

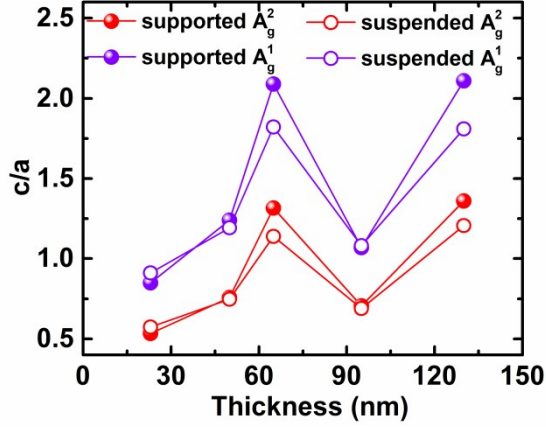


Fig. S6. The c/a -profiles of the two A_g modes of both the suspended and supported BP areas.

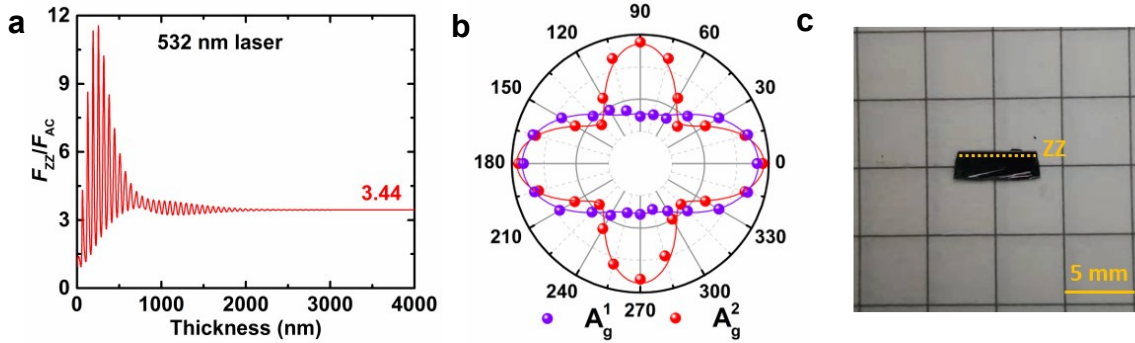


Fig. S7. (a) Calculated thickness dependent interference enhancement factor profiles (F_{ZZ}/F_{AC} - profiles) for BP on a SiO_2 (300 nm)/Si substrate for 532 nm laser by using the refractive index values of BP from ref.2. (b) The ARPRS response of the two A_g modes of bulk BP. (c) Optical image of bulk BP.

First, when the BP flake is thick enough, both the band structure and the interference enhancement factor ratio (F_{ZZ}/F_{AC}), thereby the ARPRS response (or c/a) of BP should not change with the thickness under the same excitation (in the following discussion, 532 nm excitation is used as an example). However, our calculation based on F_{ZZ}/F_{AC} shows that due to the strong linear dichroism of BP, when the thickness of BP exceeds about 4 micron, F_{ZZ}/F_{AC} no longer changes with the thickness and tends to a constant value 3.44, as shown in Fig S7a. In other words, BP with a thickness of several hundred nanometers still cannot be treated as bulk BP. Because even though their band structure may have been very close to the bulk BP at this thickness and no

longer change with thickness, the external factor F_{ZZ}/F_{AC} still changes significantly with the thickness.

Secondly, we need to note that even for bulk BP, its ARPRS response still does not represent the intrinsic response. In other words, the measured c/a is not intrinsic, because F_{ZZ}/F_{AC} for bulk BP is not 1 but 3.44, that is, the anisotropic interference effect still exists. But theoretically, we can derive the intrinsic c/a value by eqn (8) ($c^i/a^i = (c^m/a^m)/\sqrt{(F_{ZZ}/F_{AC})}$) in the manuscript. To prove this, we performed ARPRS measurement on bulk BP (Fig S7c), and its ARPRS responses of both A_g modes are shown in Fig S7b. The fitted c^m/a^m values are 1.54 and 1.02 for the A_g^1 and A_g^2 modes, respectively. Therefore, the intrinsic c/a values (c^i/a^i) are 0.83 and 0.55 for the A_g^1 and A_g^2 modes, respectively, which is consistent well with the intrinsic c/a value (~ 0.9 for A_g^1 and ~ 0.5 for A_g^2) obtained from thin BP regions in our manuscript. This consistency strongly proves the correctness of our analysis method and the potential for quantitative analysis. Also this once again reveals the important role of anisotropic interference effects in BP's ARPRS response even for bulk BP.

Thirdly, the conclusion in the manuscript also applies to bulk BP. It can be easily seen from Fig S7b that the inequality $I_{A_g^2}^{AC}/I_{A_g^1}^{AC} > I_{A_g^2}^{ZZ}/I_{A_g^1}^{ZZ}$ still holds for bulk BP. This further proves the effectiveness of our crystal orientation determination method for BP.

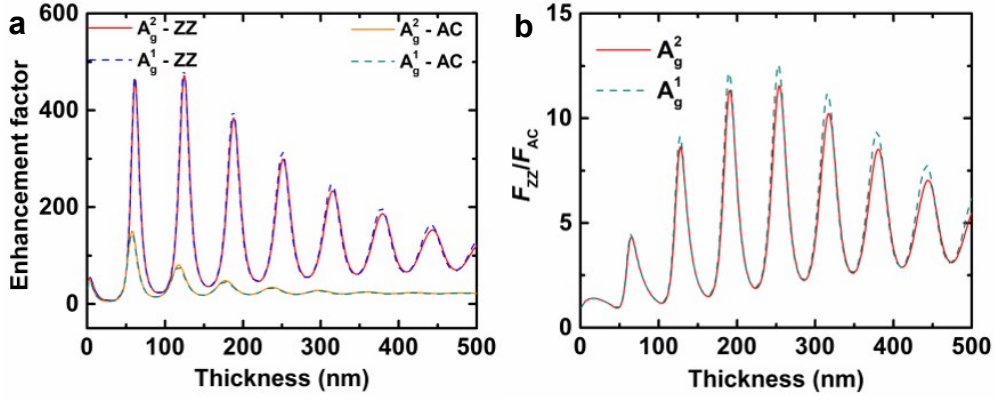


Fig. S8. (a) F_{ZZ} and F_{AC} and (b) F_{ZZ}/F_{AC} calculated by using the Raman scattering wavelengths of A_g^1 , A_g^2 modes and the corresponding wavelength-dependent complex refractive indices as shown in Table S2.

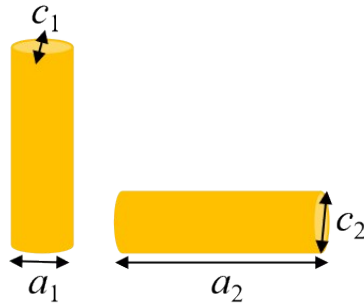
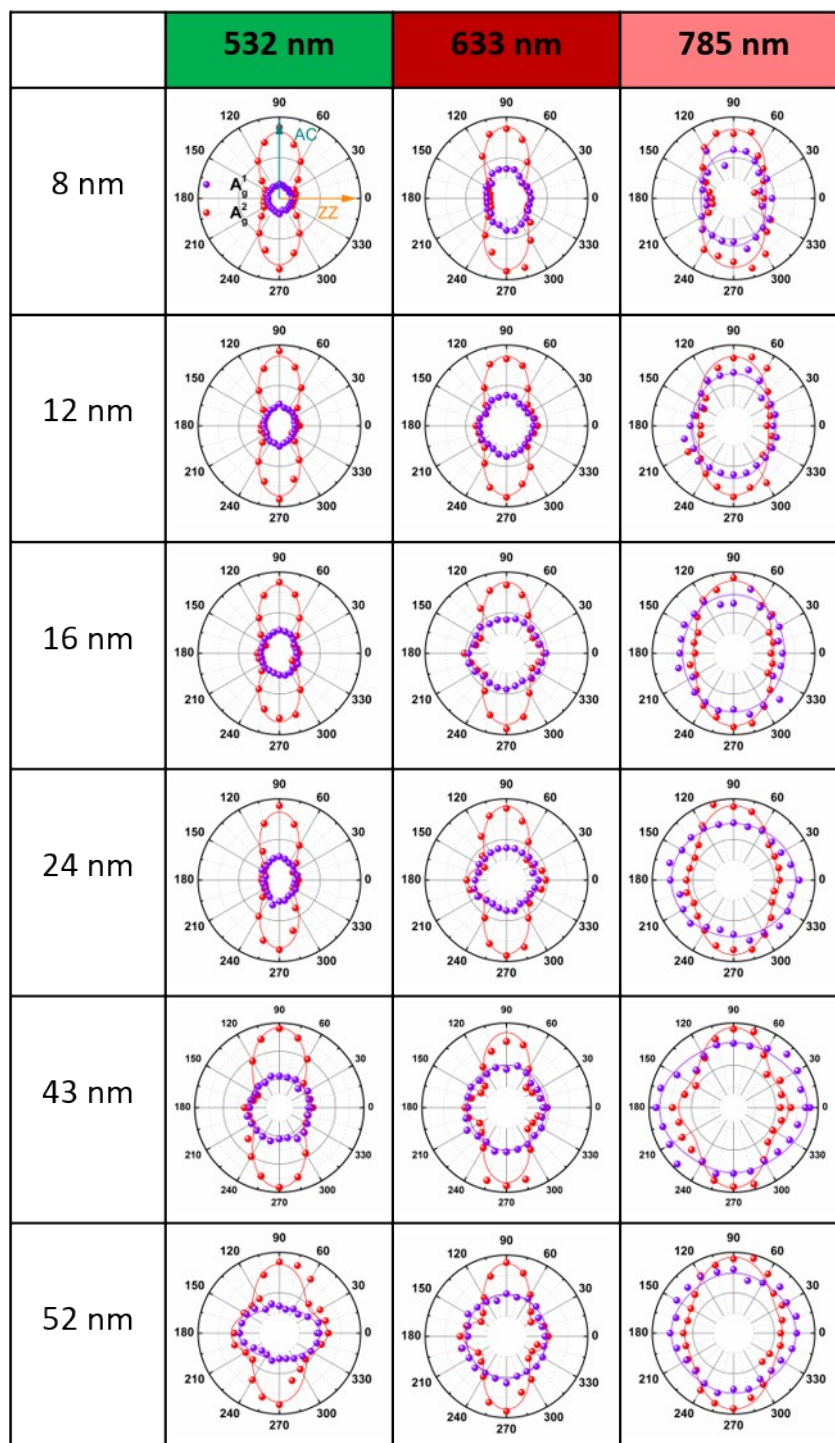
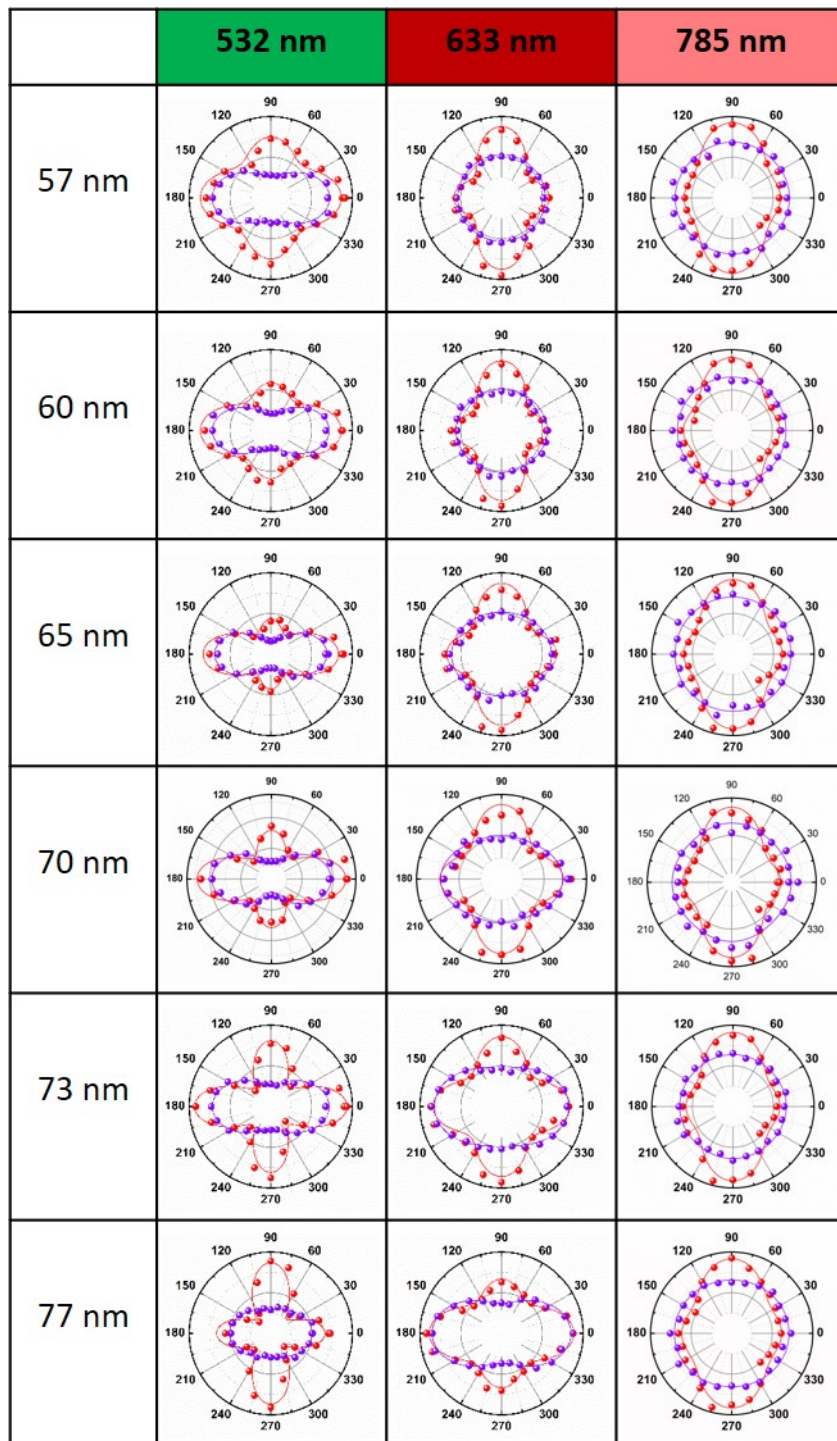


Fig. S9. Schematic diagram of the spatial distribution of the charge density difference for A_g^1 (left) and A_g^2 (right) modes.

For the A_g^1 mode of out-of-plane vibration, the electron cloud induced by the displacement of the phosphorus atom is mainly along the out-of-plane direction, which is simplified as a standing cylinder. On the contrary, for the A_g^2 mode vibrating in the in-plane AC direction, the electron cloud mainly follows the in-plane AC direction, which is simplified as a lying cylinder. In this way, we can easily find “ $a_2 > a_1$ ” and “ $c_2 \approx c_1$ ” (a_2 represents the height of the cylinder and a_1 , c_1 , c_2 represent the diameter of the cylinder).

Table S1. Polarized Raman responses of BP flakes ranging from 8-170 nm under different incident laser wavelengths.





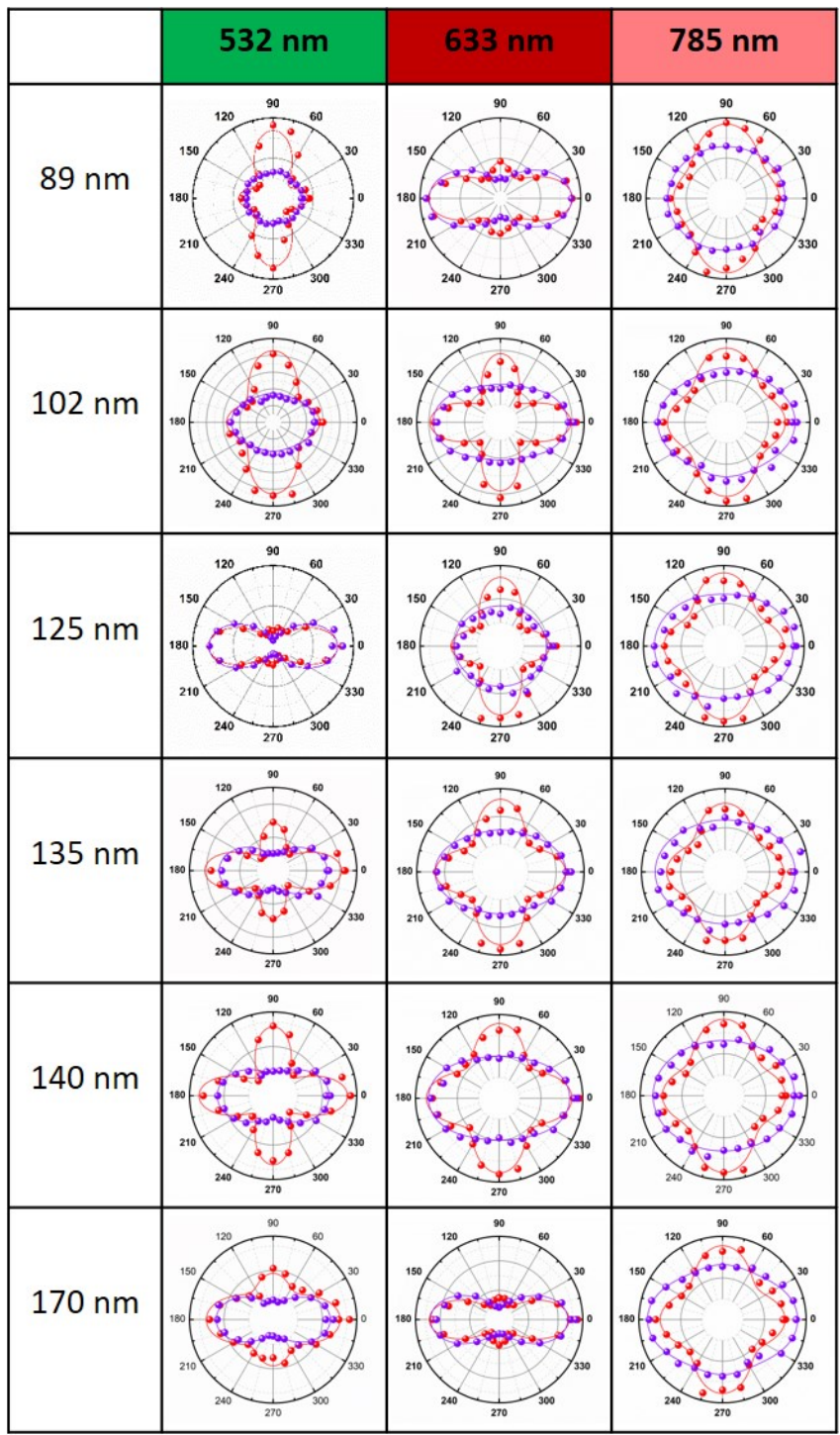


Table S2. Wavelength-dependent complex refractive indices used in the calculation of interference enhancement factor.

Wavelength (nm)	BP (zigzag) ³	BP (armchair) ³	SiO ₂ ⁷	Si ⁸
532.0	4.284-0.117i	4.547-0.357i	1.46	4.21-0.0100i
542.4	4.241-0.096i	4.491-0.334i	1.46	4.10-0.0077i
545.5	4.220-0.094i	4.469-0.315i	1.46	4.22-0.0075i
632.8	3.988-0.062i	4.179-0.247i	1.46	4.14-0.0010i
647.6	3.973-0.062i	4.149-0.235i	1.46	4.16-0.0015i
652.0	3.971-0.054i	4.145-0.241i	1.46	4.09-0.0016i
785.0	3.845-0.028i	3.993-0.224i	1.46	3.71-0.0070i
807.9	3.823-0.033i	3.977-0.215i	1.46	3.69-0.0060i
814.8	3.798-0.035i	3.965-0.218i	1.46	3.68-0.0060i

Table S3. Wavelength-dependent intrinsic Raman tensor of A_g^1 and A_g^2 modes.

Wavelength (nm)	Calculated Raman tensor		Theoretical		Experimental	
	A_g^1	A_g^2	a_2/a_1	c_2/c_1	a_2/a_1	c_2/c_1
532.0	$\begin{pmatrix} 61.8 & 0 & 0 \\ 0 & 7.1 & 0 \\ 0 & 0 & 49.4 \end{pmatrix}$	$\begin{pmatrix} 97.0 & 0 & 0 \\ 0 & 0.1 & 0 \\ 0 & 0 & 51.3 \end{pmatrix}$	1.57	1.04	1.70	1.10
632.8	$\begin{pmatrix} 35.2 & 0 & 0 \\ 0 & 7.9 & 0 \\ 0 & 0 & 14.2 \end{pmatrix}$	$\begin{pmatrix} 76.9 & 0 & 0 \\ 0 & 0.4 & 0 \\ 0 & 0 & 19.7 \end{pmatrix}$	2.18	1.39	1.30	1.00
785.0	$\begin{pmatrix} 17.5 & 0 & 0 \\ 0 & 6.2 & 0 \\ 0 & 0 & 8.0 \end{pmatrix}$	$\begin{pmatrix} 20.9 & 0 & 0 \\ 0 & 0.5 & 0 \\ 0 & 0 & 6.7 \end{pmatrix}$	1.19	0.84	1.15	0.90

Reference

1. C. Kranert, C. Sturm, R. Schmidt-Grund and M. Grundmann, *Phys Rev Lett*, 2016, **116**, 127401.
2. H. B. Ribeiro, M. A. Pimenta, C. J. S. de Matos, R. L. Moreira, A. S. Rodin, J. D. Zapata, E. A. T. de Souza and A. H. Castro Neto, *ACS Nano*, 2015, **9**, 4270-4276.
3. R. Schuster, J. Trinckauf, C. Habenicht, M. Knupfer and B. Buchner, *Phys. Rev. Lett.*, 2015, **115**, 026404.
4. M.-L. Lin, Y.-C. Leng, X. Cong, D. Meng, J. Wang, X.-L. Li, B. Yu, X.-L. Liu, X.-F. Yu and P.-H. Tan, *Sci. Bull.*, 2020, **65**, 1894-1900.
5. N. Mao, J. Tang, L. Xie, J. Wu, B. Han, J. Lin, S. Deng, W. Ji, H. Xu, K. Liu, L. Tong and J. Zhang, *J. Am. Chem. Soc.*, 2016, **138**, 300-305.
6. H. Asahina and A. Morita, *J. Phys. C Solid State Phys.*, 1984, **17**, 1839.
7. I. H. Malitson, *J. Opt. Soc. Am.*, 1965, **55**, 1205.
8. G. Vuye, S. Fisson, V. Nguyen Van, Y. Wang, J. Rivory and F. Abelès, *Thin Solid Films*, 1993, **233**, 166.